Geochemical Transactions

RESEARCH Open Access

Effect of Mn^{2+} concentration on the growth of δ-MnO_2 crystals under acidic conditions

Liyan Bi[1], Haoran Hu[1], Lei Wang[1], Zuran Li[2], Fangdong Zhan[1], Yongmei He[1], Yanqun Zu[1], Yuan Li[1*] and Xinran Liang[1*]

Abstract

δ-MnO_2 is an important component of environmental minerals and is among the strongest sorbents and oxidants. The crystalline morphology of δ-MnO_2 is one of the key factors affecting its reactivity. In this work, δ-MnO_2 was initially synthesized and placed in an acidic environment to react with Mn^{2+} and undergo a crystalline transformation. During the transformation of crystalline δ-MnO_2, kinetic sampling was conducted, followed by analyses of the structures and morphologies of the samples. The results showed that at pH 2.5 and 4, δ-MnO_2 nanoflakes spontaneously self-assembled into nanoribbons via edge-to-edge assembly in the initial stage. Subsequently, these nanoribbons attached to each other to form primary nanorods through a face-to-face assembly along the *c*-axis. These primary nanorods then assembled along the (001) planes and lateral surfaces, achieving further growth and thickening. Since a lower pH is more favorable for the formation of vacancies in δ-MnO_2, δ-MnO_2 can rapidly adsorb Mn^{2+} directly onto the vacancies to form tunnel walls. At the same time, the rapid formation of the tunnel walls leads to a quick establishment of hydrogen bonding between adjacent nanoribbons, enabling the assembly of these nanoribbons into primary nanorods. Therefore, in a solution with the same concentration of Mn^{2+}, the structure transformation and morphology evolution of δ-MnO_2 to α-MnO_2 occur faster at pH 2.5 than at pH 4. These findings provide insights into the mechanism for crystal growth from layer-based to tunnel-based nanorods and methods for efficient and controlled syntheses of nanomaterials.

Introduction

α-MnO_2 is the predominant manganese oxide in the supergene oxidation zones of manganese-bearing crusts, manganese deposits, and lateritic weathered profiles [1–4]. Representing a significant group within the transition metal oxides (TMOs), α-MnO_2 features 2×2 and 1×1 tunnel structures (with occasional intergrowth of 2×3, 2×4, and "T" junction structures), which arise from double chains of edge-sharing [MnO_6] octahedra corner-sharing with neighboring chains [5–7]. These larger tunnels are typically stabilized by cations such as K^+, Ba^+, and Na^+ [8–12]. The unique physicochemical properties of α-MnO_2, including its distinct structural and morphological characteristics, enable a broad spectrum of potential applications in environmental pollution abatement, supercapacitors, and molecular sieves [13–16]. The efficacy of these applications is significantly influenced by the specific structure and morphology of α-MnO_2 [7].

Previous research has revealed that α-MnO_2 forms from the transformation of δ-MnO_2 in acidic environments (pH<4) [7, 17–19]. δ-MnO_2 is naturally formed and widely present in nature [20]. It has poorly crystalline, *c*-axis disorder stacked [MnO_6] octahedral

*Correspondence:
Yuan Li
liyuan@ynau.edu.cn
Xinran Liang
lxr8900@live.com
[1]College of Resources and Environment, Yunnan Agricultural University, Kunming 650201, China
[2]College of Horticulture and Landscape, Yunnan Agricultural University, Kunming 650201, China

layered structure, strong adsorption and oxidation activity [21–24]. Our previous study on the one-step synthesis of α-MnO_2 revealed that the initially formed δ-MnO_2, driven by an increase in internal Mn(III), undergoes a multi-stage oriented assembly of δ-MnO_2 nanosheets, ultimately leading to the formation of α-MnO_2 nanorods [7]. Grangeon et al. through aging experiments of δ-MnO_2 with pH 3–10, found that only the δ-MnO_2 at pH 3 transformed into α-MnO_2 after four years of aging [17]. Above all, the coupled structural and morphological evolution from δ-MnO_2 to α-MnO_2 is influenced by both pH and Mn(III), although the specifics of this influence remain unclear. Understanding the morphological evolution throughout the entire synthetic process and its relationship with structural transformation, as well as the influence of pH and Mn(III) on the morphological evolution during the transformation from δ-MnO_2 to α-MnO_2, is critical for α-MnO_2 material synthesis in various applications and for understanding the mineralogy and behavior of different types of MnO_2 minerals in nature [8–16, 20, 23–27].

In this study, poorly crystalline δ-MnO_2 was synthesized. We investigate the influence of pH and Mn^{2+} on the structural transformation and morphological evolution of δ-MnO_2 into α-MnO_2 by introducing varying concentrations of Mn^{2+} at pH 2.5 and pH 4 solutions. The transformation process was observed with morphology and kinetic analyses to study the mechanism. The changes in the nanoparticle morphology and structure during the transformation of δ-MnO_2 to α-MnO_2 were observed by X-ray diffraction (XRD) and high-resolution transmission electron microscopy (HRTEM). This provides not only insights into the formation process of α-MnO_2 nanorods but also new possibilities for controlled synthesis of α-MnO_2 materials.

Experimental section

Experimental materials and methods

Reagents used in the experiment

The reagents used in this experiment included $NaMnO_4{\cdot}H_2O$ (>97%), $MnSO_4{\cdot}H_2O$ (>99%), and Hac (>97%), all of which were purchased from Sigma-Aldrich (St Louis, MO). Distilled deionized water (DDW) was used in the preparations of mineral reagents and for washing the products. The DDW was obtained by treating distilled water with a Labconco Water Pro Ps system, and the resulting resistivity was greater than 18.4 MΩ•cm.

Synthesis of poorly crystalline δ-MnO2

In a typical experiment, 10.00 g $NaMnO_4$ was dissolved in 680 mL of 0.25 mol/L NaOH solution. Then, 320 mL of 0.3 mol/L $MnCl_2$ solution was added to the $NaMnO_4$ solution dropwise at a rate of 10.00 mL/min. The suspension was vigorously stirred for an additional 2 h and then standing for 4 h. The precipitate which obtained after centrifugation was mixed with 1 M $NaCl_2$ solution for 1 h. The suspension was filtered and washed until the conductivity of the supernatant was less than 20.0 μS cm^{-1} [7].

Isothermal adsorption

The isothermal adsorption experiments were controlled variable experiments, and the controllable factors in this experiment were the concentration of Mn^{2+} and the pH of the solution. To meet the quantity requirements for subsequent characteristics, we ultimately adopted the 3 g/L δ-MnO_2 suspension concentration reported by Zhao et al., as determined through our preliminary experiments [28]. The pH setting is based on the findings reported by Grangeon et al. that transformation from δ-MnO_2 to α-MnO_2 is more favorable at pH values below 4, and does not occur at pH 5 [19]. Therefore, we set the pH levels to 2.5, 4, and 5. Our previous research found that δ-MnO_2 can transform into α-MnO_2 when the Mn(III) content above and below the vacancies is at 30%. We used this as the median concentration to set higher and lower Mn^{2+} concentrations to study their effects on the transformation process [7]. The concentrations of Mn^{2+} were 0 mol/L, 0.05 mmol/L, 0.1 mmol/L, 0.3 mmol/L, 0.7 mmol/L, 1 mmol/L, 5 mmol/L, 10 mmol/L, 25 mmol/L, and 50 mmol/L. There were 3 groups of experiments (Table 1). Each set of experiments was repeated three times, and the average value was taken.

For each sample, 2.5 mL of 36 g/L suspension of poorly crystalline δ-MnO_2 was added to a centrifuge tube with a certain amount of $MnSO_4$ solution and a certain volume of deionized water. The total volume of the solution was 30 mL. The pH of the mineral suspensions was adjusted to 0.01 mol/L, 0.05 mol/L, 0.1 mol/L, 0.5 mol/L, 1.00 mol/L NaOH and H_2SO_4. The changes in the suspension pH were regularly monitored, the set pH was maintained, and the mixture was allowed to react for several

Table 1 Experimental settings of the parameters in the syntheses

Experimental group	①[1)]	②[1)]	③[1)]	④[1)]	⑤[1)]	⑥[1)]	⑦[2)]	⑧[2)]	⑨[2)]	⑩[2)]
C(Mn^{2+}) mmol/L	0	0.05	0.1	0.3	0.7	1	5	10	25	50
V(Mn^{2+}) mL	0	0.5	1	3	7	10	1	2	5	10
V(DW) mL	27.5	27	26.5	24.5	20.5	17.5	26.5	25.5	22.5	17.5

Note: (1) The concentration of the added $MnSO_4$ solution was 3 mmol/L; (2) the concentration of the added $MnSO_4$ solution was 0.15 mol/L

days until the pH change was less than ±0.05 within 7 days. After 7 days of stirring, the sample was centrifuged once in a centrifuge tube, the supernatant was removed, and the sample was washed and centrifuged several times until the conductivity of the supernatant was 20 μS/cm. After centrifugation, a high-speed freezing centrifuge (BECKMAN J2-MC) was used at relative centrifugal force (RCF) of 17,800 g, and the centrifugation time was 6 min. The washed paste was freeze-dried, ground in an agate mortar and then bottled for later use. The concentration of Mn^{2+} in the supernatant after centrifugation was determined with flame atomic absorption spectroscopy, and the amount of Mn^{2+} adsorbed and its maximum adsorption capacity were determined at different pHs. Each set of experiments was repeated three times, and the average value was taken.

Kinetics experiments

Briefly, 3 g of wet δ-MnO_2 (the weight of the solid sample is 0.624 g) was transferred to 200 mL of deionized water containing 25 mM $MnSO_4$. Then the pH of suspension was maintained at ~ 2.5 or 4 for 15 d under vigorous stirring by addition of 0.1 M NaOH or 0.1 M H_2SO_4. Aliquots were taken at various time intervals and the solids were collected by centrifugation at 16 000 g (Neofuge 23R). The collected solids were then rinsed with DDW until the supernatant conductivity was below 20 μS/cm.

Characterization

X-ray diffraction (XRD) analyses of minerals

The synthesized manganese oxide minerals or intermediates were completely washed with DDW, and then X-ray diffraction (XRD) analyses were carried out with a D8 ADVANCE instrument from the BRUKER Company in Germany. Powder tableting and directional tableting processes were used. The test conditions were as follows: Cu Ka radiation (λ=0.15406 nm), a 40 kV test voltage, a 40 mA test current, steps, 10°/min scanning speed, and 0.01° step sizes.

Transmission electron microscopy (TEM)

The morphologies and crystalline characteristics of the minerals were analyzed with an FEI-Talos-F200 analytical transmission electron microscope (TEM) and identified by electron diffraction (ED). The acceleration voltage was 200 kV, and the emission current was 10 μA. Ten mL of the sample was added to anhydrous ethanol in a 20 mL capacity serum bottle, small amounts of minerals were added to anhydrous ethanol, and after ultrasonic dispersion, the solution was slightly discolored. Samples were taken from the suspension with an ultrathin carbon membrane for computer analyses.

Flame atomic absorption spectrometry

The concentrations of Mn^{2+} in the solutions were determined with a Varian AAS240 FS atomic absorption spectrometer. The corresponding elemental lamps and standard curves were used for analyses.

Results and analysis

Mn2+ adsorption at different pH

As shown in Fig. 1a, the amount of Mn^{2+} adsorbed under acidic conditions increased with the addition of the same amount of Mn^{2+} and with an increase in pH. When the initial concentration of Mn^{2+} in the solution was less than 5 mmol/L, δ-MnO_2 was completely adsorbed at both pH 2.5 and 4. However, as the concentration of Mn^{2+} in the solution continued to increase, the adsorption of Mn^{2+}

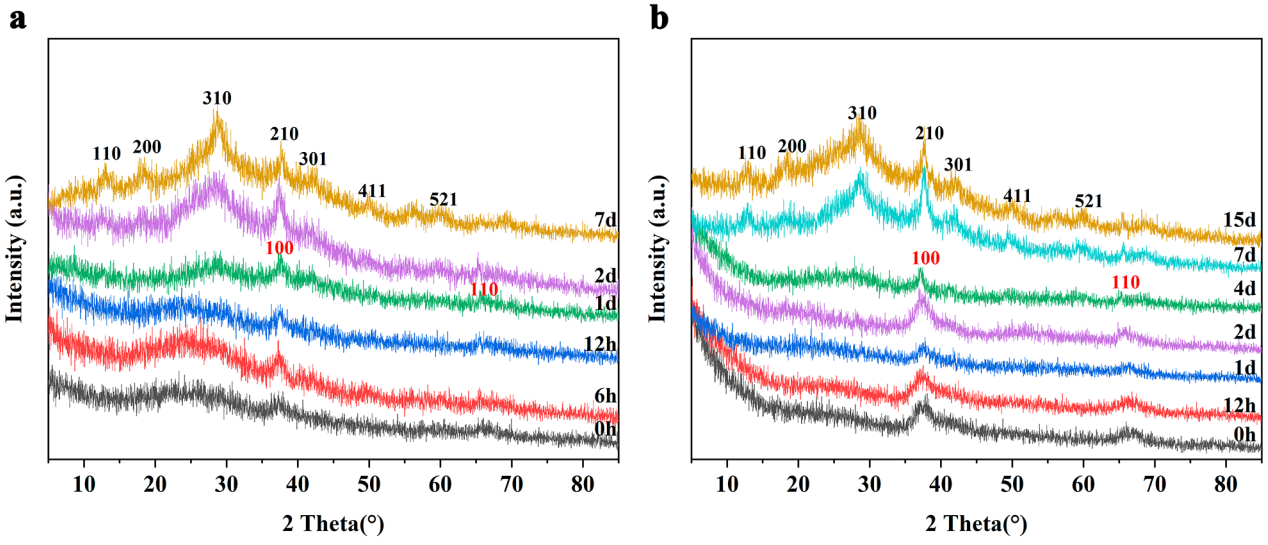

Fig. 1 Isothermal adsorption experiments of δ-MnO_2 on Mn^{2+} in solutions with pH 2.5 and 4 (**a**), adsorption kinetics of δ-MnO_2 in a 25 mM Mn^{2+} solution (**b**)

by δ-MnO_2 reached saturation at pH 2.5. At pH 4, the adsorption of Mn^{2+} by δ-MnO_2 reached saturation when the concentration of Mn^{2+} reached 22.5 mmol/L. This is attributed to the point of zero charge (PZC) of δ-MnO_2, which ranges between 1.5 and 2.5. With the increased pH, the negative charge on δ-MnO_2 also increased, subsequently enhancing its Mn^{2+} adsorption capacity. Notably, the maximum adsorption capacity for Mn^{2+} is lower at pH 2.5 than that at pH 4.

We conducted kinetic experiments using 25 mM Mn^{2+} with 3 g/L δ-MnO_2, and the results are shown in Fig. 1b. When the solution had a pH of 2.5 and 4, the concentration of Mn^{2+} in the solution rapidly decreased from 25 mM to 2.5 mM and 3.6 mM after the addition, respectively. The kinetic process of δ-MnO_2 adsorbing Mn^{2+} can be divided into two parts. Initially, in the first 48 h, the adsorption of Mn^{2+} by δ-MnO_2 showed minor fluctuations, indicating instability in the adsorption of Mn^{2+} during this phase. This is likely due to Mn^{2+} continuously undergoing electron transfer with δ-MnO_2 and exchanging with Mn (IV) in bulk, which promotes the crystallization and structural transformation of δ-MnO_2 [29, 30]. Subsequently, in the second part, from 48 h to 15 days, the amount of Mn^{2+} adsorbed by δ-MnO_2 gradually increased over time. The distinctly different two-stage adsorption process is likely due to the structural and morphological evolution of δ-MnO_2 caused by Mn^{2+}.

XRD patterns of the isothermal adsorption sample

The XRD pattern of the sample obtained after 15 d of reaction is shown in Fig. 2. The XRD pattern of the samples when the Mn^{2+} concentrations were 0, 1 mmol/L and 5 mmol/L shows two broad diffraction peaks at 37° ($d_{(100)}$=0.24 nm) and 65° ($d_{(110)}$=0.14 nm) (Fig. 2), which can be attributed to δ-MnO_2 with poor crystallinity, small-sized and randomly stacked [MnO_6] octahedral layers [21, 22]. The *d*-spacing ratio of $d_{(100)}$ to $d_{(110)}$ is 1.73, which indicates a hexagonal layer symmetry [21]. When Mn^{2+} was added up to 10 mmol/L, the peak at $d_{(100)}$=0.24 nm began to sharpen and a new shoulder peak appeared at 42.2° 2θ, indicating that Mn^{2+} was gradually adsorbed on the top and bottom of the octahedral vacancies (Fig. 2). When Mn^{2+} was added to more than 25 mmol/L, (110), (200), and (310) α-MnO_2 peaks appeared (ICDD No. 00-29-1020, $d_{(110)}$=0.69 nm, $d_{(200)}$=0.48 nm, and $d_{(310)}$=0.31 nm) (Fig. 2). In the isothermal adsorption curve, when the concentration of Mn^{2+} in the solution reached 10 mmol/L, the adsorption capacity of δ-MnO_2 for Mn^{2+} was close to saturation (Fig. 1a). In the XRD patterns, even in this state of adsorption saturation, δ-MnO_2 did not undergo structural transformation. As more Mn^{2+} was added, the amount of Mn^{2+} adsorbed by δ-MnO_2 did not change significantly, but δ-MnO_2 transformed into α-MnO_2 structure. It might be because the appropriate amount of Mn^{2+} did not directly integrate into δ-MnO_2, but rather facilitated the transformation of δ-MnO_2 to α-MnO_2 through its effect on the electron transfer of surface Mn (III/IV).

XRD patterns of the adsorption kinetics samples

The XRD patterns of the obtained samples under pH 2.5 are shown in Fig. 3. The initial mineral was poorly crystalline δ-MnO_2. After 2 days of reaction, the intensity of the diffraction peak at *d*=0.24 nm increased. And at the same time, the characteristic diffraction peak of α-MnO_2 ($d_{(110)}$=0.70 nm) appeared at 12° 2θ, which indicated that δ-MnO_2 was transformed into α-MnO_2 after 2 days (Fig. 2a) [7, 11]. When the reaction time was extended

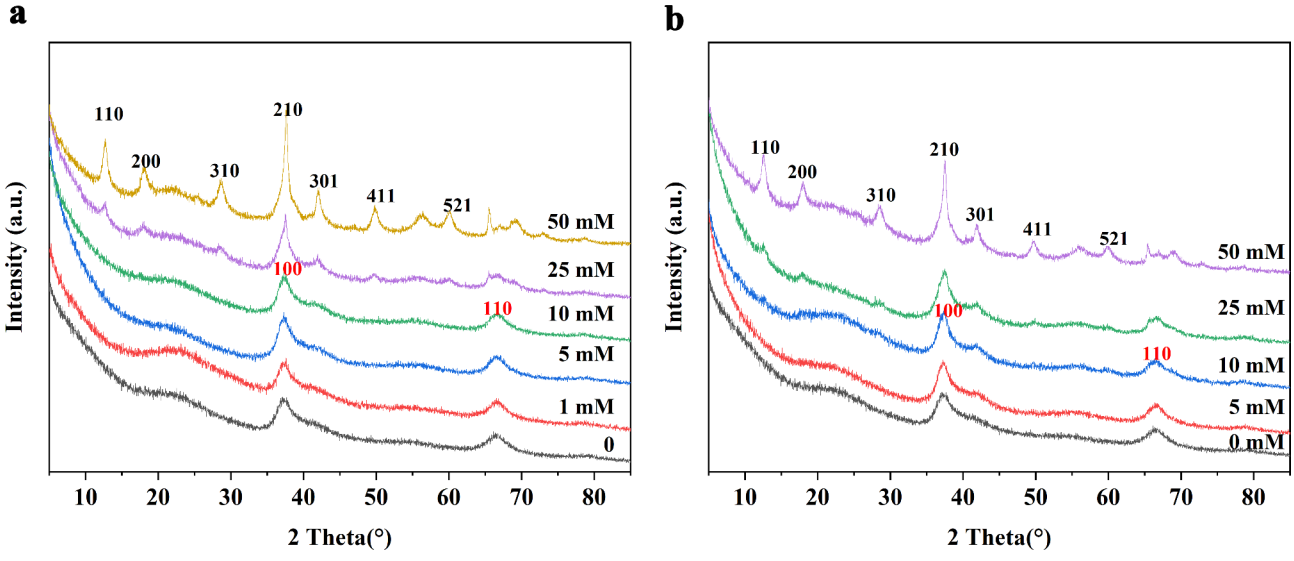

Fig. 2 The XRD patterns of solid samples in isothermal adsorption experiments of δ-MnO_2 on Mn^{2+} in solutions with pH 2.5 (**a**) and 4 (**b**)

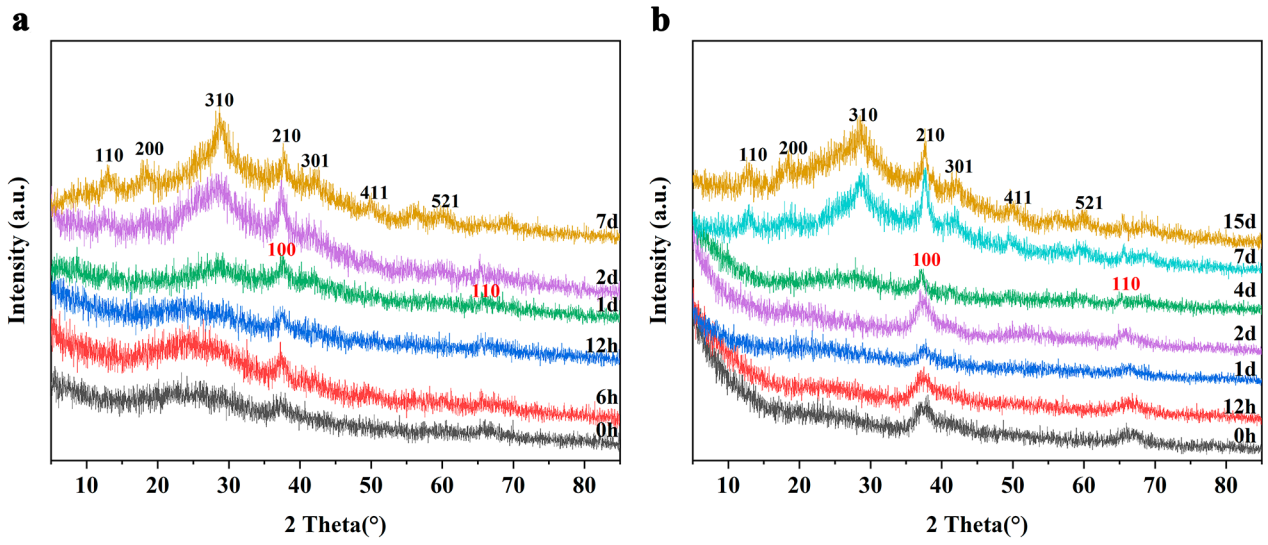

Fig. 3 The XRD patterns of solid samples in adsorption kinetics experiments of 25 mM Mn^{2+} on δ-MnO_2 in solutions with pH 2.5 (**a**) and 4 (**b**)

to 7 days, the intensity of the diffraction peak gradually increased indicated that the δ-MnO_2 transformed into α-MnO_2 (Fig. 2a). Before the transformation, δ-MnO_2 continuously exchanged with Mn^{2+} in the solution, preparing for the conversion to α-MnO_2, such as the generation and arrangement of Mn (III) [7]. Therefore, the adsorption amount of Mn^{2+} by δ-MnO_2 was constantly fluctuating. When the reaction proceeded for two days, δ-MnO_2 transformed into the more stable α-MnO_2, and α-MnO_2 further adsorbed Mn^{2+} from the solution.

The XRD patterns of the samples, capturing the dynamic interaction between δ-MnO_2 and 25 mM Mn^{2+} in a pH 4 solution over a period of 15 days, are shown in the Fig. 3b. Compared to the rate at which δ-MnO_2 begins to convert to α-MnO_2 within 2 days in a pH 2.5 solution, δ-MnO_2 in a pH 4 solution only starts to transform into α- MnO_2 after 7 d. When the reaction time was 4 days, the peak intensity of $d_{(100)}$=0.24 nm increased, indicating that the crystallinity of the δ-MnO_2 increased with increasing reaction time [18]. When the reaction time was extended to 7 days, the peak intensity at d=0.24 nm increased, and the characteristic diffraction peak for α-MnO_2 ($d_{(110)}$=0.70 nm) appeared at 2θ=12°. This indicated that after 7 days, δ-MnO_2 transformed into α-MnO_2 [7, 11]. Therefore, compared to the reaction system at pH 2.5, δ-MnO_2 in pH 4 exhibits a fluctuation cycle (preparation period) of 7 days in Mn^{2+} adsorption. An increase in adsorption is observed when δ-MnO_2 begins its transformation into α-MnO_2 on the 7 days.

Morphological changes of δ-MnO2 under different pH

Morphological of initial δ-MnO2

Figure 4a illustrates the initial formation of nanoflakes aggregates upon mixing the $KMnO_4$ and $MnSO_4$ solutions. Further captured at a higher resolution (Fig. 4b), reveals poorly crystalline δ-MnO_2 nanosheets ranging in size from 3 to 5 nm, featuring a lattice spacing of $d_{(100)}$=0.24 nm. Furthermore, the selected area diffraction (SAED) pattern (inset of Fig. 4a) shows two diffuse diffraction rings at ~0.24 nm and ~0.14 nm, which is consistent with the $d_{(100)}$=0.24 nm and $d_{(110)}$=0.14 nm spacings of δ-MnO_2, respectively. This observation consists with the results obtained from XRD pattern in Fig. 3.

Morphological changes of δ-MnO2 under pH 2.5

When δ-MnO_2 reacted with Mn^{2+} for 1 h at pH 2.5, as demonstrated in Fig. 5a and b, nanoribbons with lengths of 10–20 nm were formed. Upon magnifying nanoribbons, it becomes revealed that these nanoribbons are assembled from several δ-MnO_2 nanoflakes. They display lattice with a spacing of $d_{(100)}$=0.24 nm, while lacking the typical lattice spacing of d=0.7 nm characteristic of α-MnO_2. This indicates that these nanoribbons are assembled δ-MnO_2.

When the reaction time was extended to 1 day, as shown in Fig. 5c and d, the δ-MnO_2 nanoflakes gradually disappeared, while the nanoribbons increased in length to 100 nm. The δ-MnO_2 nanoflakes were gradually transforming into δ-MnO_2 nanoribbons as there were no lattice stripes of α-MnO_2 observed. The side perspective of a nanoribbon highlight by yellow dashed line in Fig. 5d demonstrates that an δ-MnO_2 nanoflake assemble at the end surface of a nanoribbon.

When the reaction time was extended to 4 days, the δ-MnO_2 nanoflakes almost disappeared, resulting in the formation of nanorods with good crystallinity and lengths ranging from 100 nm to 300 nm (Fig. 6a). Upon further magnification of the nanorods, the lattice with

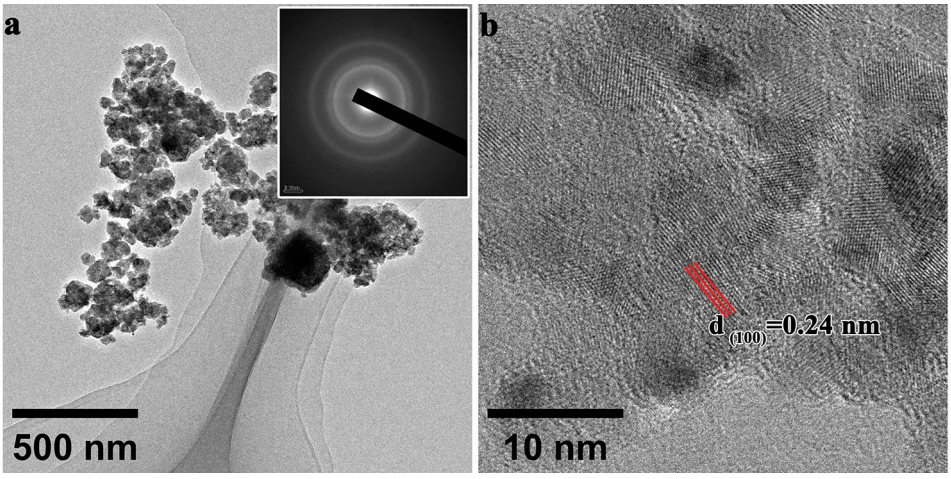

Fig. 4 TEM images of the intermediate product of initial δ-MnO_2 (**a** and **b**) and the SAED pattern (an inset) were recorded by focusing the electron beam in the area of image **b**

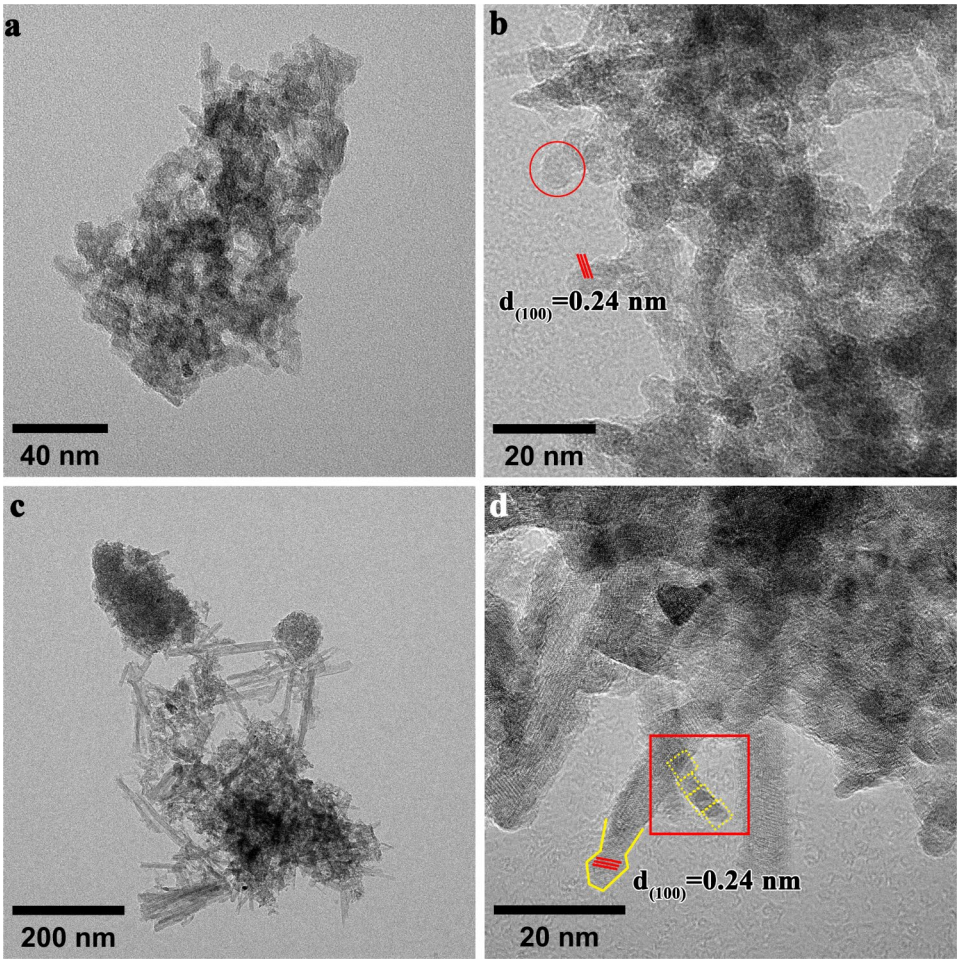

Fig. 5 TEM images of δ-MnO_2 react with 25 mM Mn^{2+} at pH 2.5 about 1 h (**a** and **b**), and 1 d (**c** and **d**). The red line and circles represent hexagonal δ-MnO_2 nanoflakes in image **b**. The yellow dashed lines within the red rectangular area show the assembly of several δ-MnO_2 nanoflakes into nanoribbons in image **d**

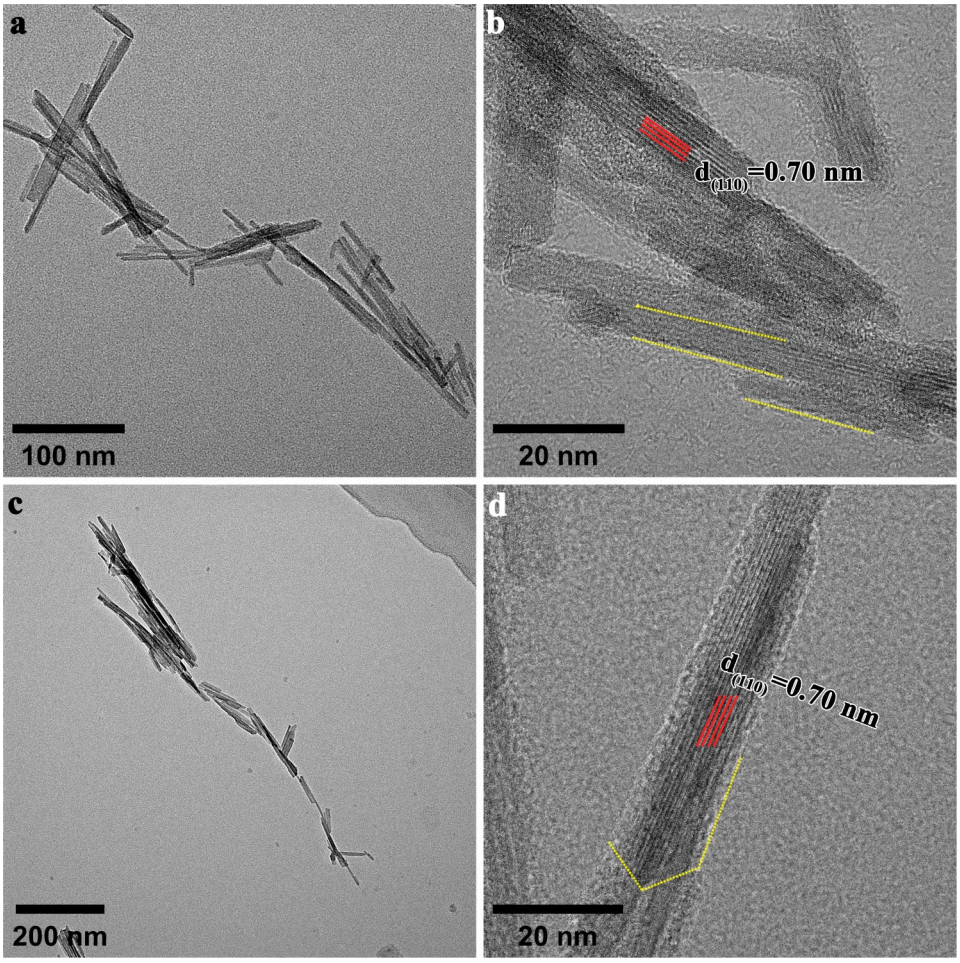

Fig. 6 TEM images of δ-MnO_2 react with 25 mM Mn^{2+} at pH 2.5 about 4 d (**a** and **b**), and 7 d (**c** and **d**). The yellow dashed lines show the side-to-side assembly in image **b**. The yellow dashed lines show the end-to-end assembly in image **d**

a spacing of $d_{(110)}$=0.70 nm characteristic of α-MnO_2 structures were observed internally (Fig. 6b), consistent with the XRD pattern (Fig. 3a). Small nanorods were assembled side-to-side with each other, increasing the thickness of the original nanorods observed in Fig. 6b. Previous studies also described this side-to-side assembly of α-MnO_2 nanorod along the (110) plane driven by surface energy [11, 21].

When the reaction time reached 7 days, the nanorods grew to approximately 400 nm and tended to grow in the same direction shown in Fig. 6c. As shown by the amplified image in Fig. 6d, short nanorods with length of about 150 nm connect with each other by end-to-end assembly along the α-MnO_2 (001) planes to form secondary nanorods.

Morphological changes of δ-MnO2 under pH 4

When all other conditions remained unchanged and only the pH value was adjusted from 2.5 to 4, nanoribbons with weak crystallinity appeared after a reaction time of 12 h shown in Fig. 7a. The internal lattice of the nanoribbon is inconsistently oriented, with spacing of $d_{(100)}$=0.24 nm, indicating that it is a δ-MnO_2 structure. These nanoribbons are approximately 40 nm in length, which is longer than the nanoribbons (length about 20 nm) formed after 1 h at a pH of 2.5. It is noteworthy that the $d_{(100)}$=0.24 nm lattice directions within the nanoribbons are inconsistent, which may be due to the δ-MnO_2 nanoribbons being newly assembled by δ-MnO_2 nanoflakes and not having the opportunity to adjust orientations (Fig. 7b).

When the reaction time reached 4 days, δ-MnO_2 nanoflakes gradually transform into nanoribbons with length from 100 to 200 nm (Fig. 7c and d). δ-MnO_2 nanoflakes were observed to assemble on the end faces of the nanoribbons (Fig. 7d). This may be due to the outside nanoflakes of the initial δ-MnO_2 nanoflakes aggregation were first assembled into long nanoribbons. Then the inner δ-MnO_2 nanoflakes were gradually involved as the reaction progressed. Therefore, δ-MnO_2 was still present after 4 days. Figure 7d shows several nanosheets stacking

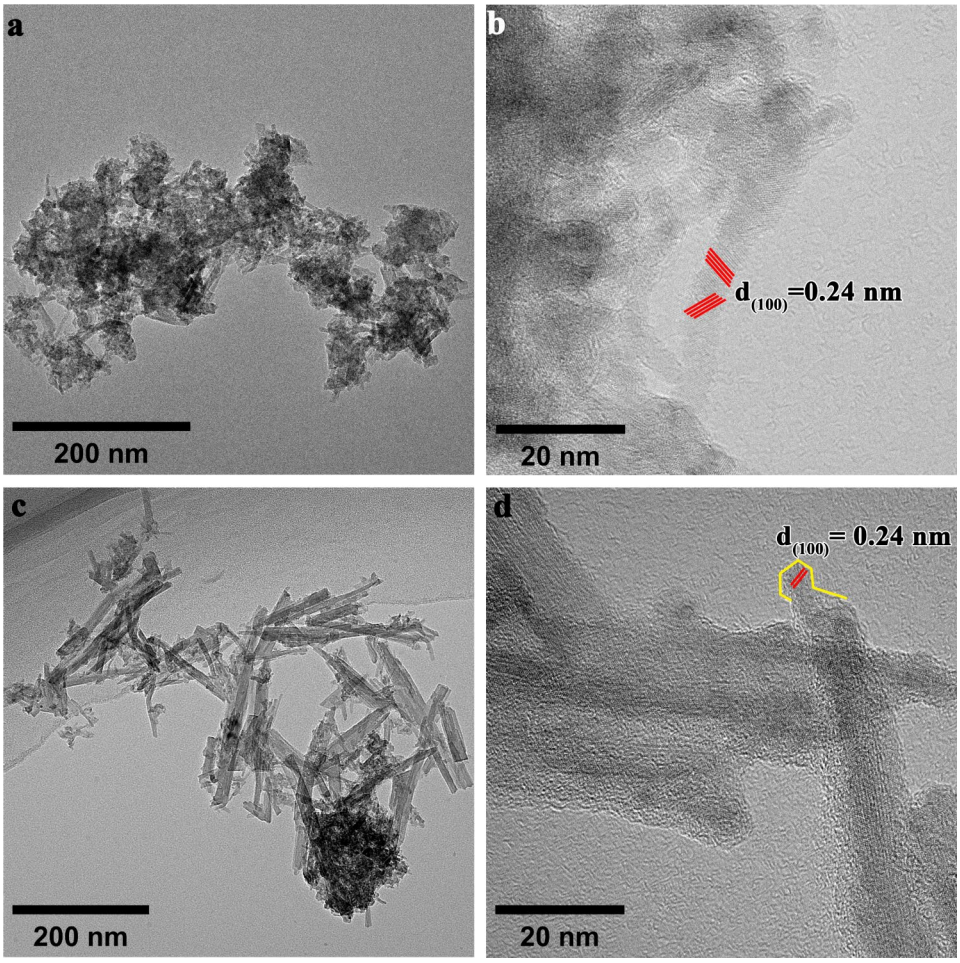

Fig. 7 TEM images of δ-MnO_2 react with 25 mM Mn^{2+} at pH 4 about 12 h (**a** and **b**), and 4 d (**c** and **d**). The yellow lines show the assembly of δ-MnO_2 nanoflakes on the end of nanoribbons in image **d**

and thickening each other, resulting in the formation of nanorods.

After 7 days of reaction, TEM observations revealed that the δ-MnO_2 nanoflakes had disappeared, and nanorods approximately 500 nm in length had emerged (Fig. 8a). The SAED with $d_{(110)}$=0.70 nm characteristic of α-MnO_2 was observed, indicating the beginning of the transformation from δ-MnO_2 to α-MnO_2 (Fig. 8b). In Fig. 8b, numerous nanoribbons (30 nm in length and 5 nm in width) were observed assembled at the end of nanorods. Notably, these nanoribbons did not exhibit lattice with a spacing of $d_{(110)}$=0.70 nm, suggesting they are still of the δ-MnO_2 structure. It is probable that these nanoribbons stacked upon each other during the assembly process, ultimately extending along the assembled faces of the nanorods and forming α-MnO_2 nanorods.

After 15 days of reaction, there are nanorods with 300–500 nm in length and 30 nm in width were formed (Fig. 8c). Upon further magnification of the nanorods, the lattice with a spacing of $d_{(110)}$=0.70 nm characteristic of α-MnO_2 structures were observed (Fig. 8d), which was consistent with the XRD findings after 15 d (Fig. 3b). Additionally, it was observed that the nanorods underwent side-to-side assembly along the (110) crystal planes, leading to an increase in width.

Discussion

$$2KMnO_4 + 3MnSO_4 + 2H_2O = 5MnO_2 + 2H_2SO_4 + K_2SO_4 \quad (1)$$

The morphological evolution process of δ-MnO_2 to α-MnO_2 in the presence of Mn^{2+} in solutions with pH 2.5 and 4 is shown in Schematic 1. As shown by the chemical reaction in Eq. (1), the initial δ-MnO_2 was produced by reducing $KMnO_4$ with $MnSO_4$. The δ-MnO_2 formed small nanoflakes about 3 to 5 nm in size with hexagonal symmetry. In pH 2.5 or pH 4 solution, δ-MnO_2 reacts with Mn^{2+} concentrations greater than 10 mM to transform into α-MnO_2 nanorods. Specifically, δ-MnO_2 nanoparticles with sizes ranging from 3 to 5 nm first assembled edge-to-edge along the (100) plane to form longer δ-MnO_2 nanoribbons [28, 31]. This is consistent

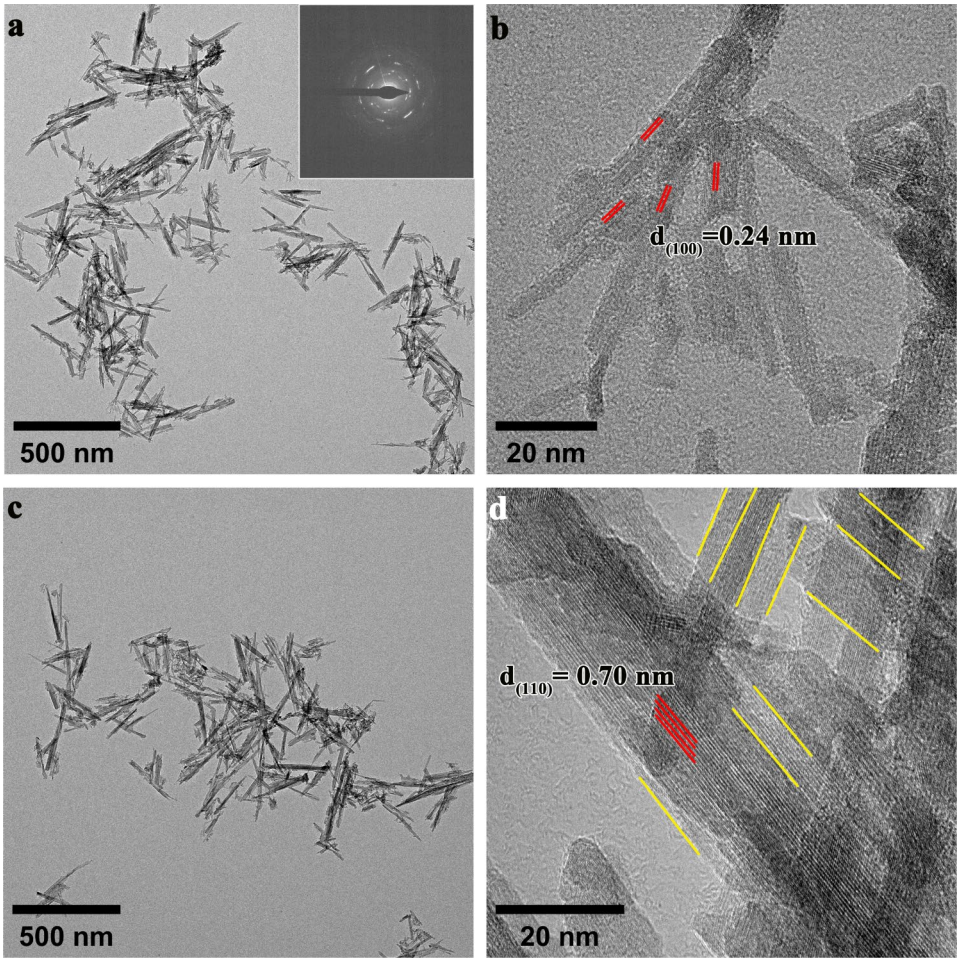

Fig. 8 TEM images of δ-MnO_2 react with 25 mM Mn^{2+} at pH 4 about 7 d (**a** and **b**), and 15 d (**c** and **d**). The SAED pattern (an inset) was recorded by focusing the electron beam in the area of image **b**. The yellow lines show the side-to-side assembly in image **d**

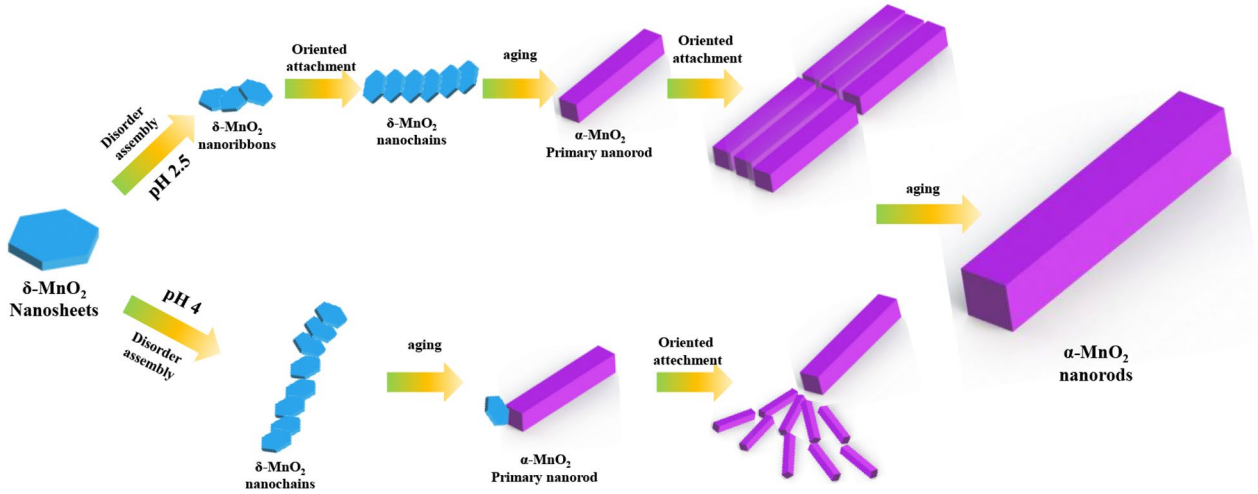

Schematic 1 Diagram of crystal growth during the transformation of δ-MnO_2 nanosheets to α-MnO_2 nanorods at different pH

with the findings of Liang et al. who reported that the morphology evolution preceded the formation of the mineral phase [7]. In pH 2.5 solution, secondary δ-MnO_2 nanoribbons were assembled along the (110) surface and thickened to form primary α-MnO_2 nanorods. Thirdly, primary α-MnO_2 nanorods assemble through end-to-end along the (001) plane to form longer nanorods. Adjacent nanorods align side-to-side along the (110) surface, driven by the high surface energy, to form wider nanorods.

Previous studies have shown that the cation adsorption capacity of δ-MnO_2 increases with the rise in pH [32, 33]. This study also reveals that the amount of Mn^{2+} adsorbed by δ-MnO_2 at pH 4 is 0.5 mmol/g greater than that in a pH 2.5 solution. The slight increase in δ-MnO_2 adsorption capacity for Mn^{2+} is the result of the combined changes in the number of vacancies and the amount of negative charge as the pH increases. A previous study revealed that after aging δ-MnO_2 for several years at various pHs, the δ-MnO_2 vacancy content was closely related to the pH, with a lower pH leading to the formation of more δ-MnO_2 vacancies [17]. The vacancies in δ-MnO_2, which have a negative charge due to charge deficiency, can strongly adsorb positively charged ions. Therefore, the number of vacancies in δ-MnO_2 at pH 2.5 is greater than in a pH 4 solution. Conversely, the PZC of δ-MnO_2 is 1.5–2.5, and as the pH of the solution increases from 2.5 to 4, the increase in negative charge leads to stronger adsorption of Mn^{2+} [33]. However, the effect of the vacancies was not as significant as that of the PZC, and the amount of Mn^{2+} adsorbed by δ-MnO_2 at pH 4 was greater than in a pH 2.5.

In this study, when there is a small difference in the amount of Mn^{2+} adsorbed by δ-MnO_2, pH is a key factor in controlling the rate of its transformation to the 2×2 tunnel structure of α-MnO_2 [32, 33]. This may be because at pH 2.5, more vacancies are formed directly, and Mn^{2+} is directly adsorbed onto these vacancies after its addition [17]. According to the reaction in Eq. 2, a large amount of [Mn (III)O_6] tunnel walls are formed. These [Mn (III)O_6] octahedra include three unsaturated oxygen molecules that combine with H^+ to form -OH. When the amount of -OH is large enough, a network of hydrogen bonds (H-bonding) forms between the [Mn (III)O_6] octahedra of adjacent nanoribbons and nanoflakes [7]. However, in a pH 4 solution, fewer vacancies are formed in δ-MnO_2 [34]. The initial adsorption of Mn^{2+} and its reaction with δ-MnO_2 generate Mn(III), which migrates onto the vacancies due to the Jahn-Teller effect [7]. This process is slower than direct adsorption onto vacancies [35]. Therefore, at a solution pH of 2.5, δ-MnO_2 begins to transform into α-MnO_2 within 2 d, while in a pH 4 solution, this process in δ-MnO_2 only starts after 7 days.

In comparison to the solution at pH 2.5, the nanoflakes in the pH 4 solution assembled to form longer nanoribbons due to the prolonged transformation process. This is because the formation of [Mn(III)O_6] tunnel walls takes longer at pH 4 compared to pH 2.5, allowing δ-MnO_2 nanoflakes enough time to assemble edge-to-edge and form longer nanoribbons [7, 36, 37]. Therefore, when these long nanoribbons have assembled enough tunnel walls, they directly form primary α-MnO_2 nanorods longer than those formed at pH 2.5. When nanoribbons are assembled to form nanorods in a pH 4 solution, many δ-MnO_2 nanoflakes remain unassembled into nanoribbons and directly assemble on the (100) crystal face of the primary nanorods. As the pH decreases, the H-bonding between -OH groups on the edges of δ-MnO_2 nanoflakes becomes stronger, resulting in the rapid assembly of smaller nanoribbons at pH 2.5. In contrast, when the primary nanorods begin to form at pH 4, some δ-MnO_2 nanosheets are still present because the H-bonding is weakened. This phenomenon continues, and subsequently, the uncompleted nanoribbons continue to assemble directly along the (100) crystal face of the nanorods.

$$Mn^{2+} + MnO_2 + 2H_2O \rightarrow 2Mn^{3+} + 2H^+ \quad (2)$$

$$2Mn^{3+} + 2H_2O \rightarrow Mn^{2+} + MnO_2 + 4H^+ \quad (3)$$

Finally, these primary α-MnO_2 nanorods assemble end-to-end and side-to-side, increasing in width and length. Yuan et al. calculated the energy of the α-MnO_2 (110) facets to be 0.74 J/m^2 and the energy of the (001) facet to be 1.17 J/m^2. Driven by the increased surface energy, the nanorods connected head-to-tail along the (001) faces and side-to-side via H-bonding at the (110) face, resulting in further thickening and growth of the α-MnO_2 nanorods [11].

In summary, these results showed that different pH values and different Mn^{2+} concentrations had significant impacts on the structural transformation and morphological evolution of δ-MnO_2 to α-MnO_2. Although this study is not exhaustive, it highlights an important area for further researches on the morphological and structural interactions under different conditions. Future studies could involve quantifying the number of vacancies at different pH levels and exploring the interactions of Mn^{2+} within the system using isotope studies. Additionally, in-situ morphological characterization techniques can be employed to determine the kinetics and mechanisms of the transformation from δ-MnO_2 nanoflakes to α-MnO_2 nanorods under different pH conditions.

Conclusion

δ-MnO_2 is a kind of 3–5 nm nanoparticles consisting of [Mn(III)O_6] octahedra and single-layer flaky manganese oxide with hexagonal symmetry and similar biological functions in a supergene environment. The amount of Mn^{2+} adsorbed by δ-MnO_2 increased with increasing pH, indicating that the negative charge on the mineral surface was greater at pH 4 than at pH 2.5, thus the rate of Mn^{2+} adsorption was greater at pH 4 than at pH 2.5. Different pH values and Mn^{2+} concentrations strongly influenced the transformation of δ-MnO_2 into α-MnO_2. As Mn^{2+} increases and pH decreases from pH 4 to 2.5, the transformation of δ-MnO_2 to α-MnO_2 nanorods accelerates. With increasing reaction time, δ-MnO_2 nanoparticles grew and thickened at the tops and edges of the nanorods through oriented attachment.

Acknowledgements
The authors thank the Youth Project of Yunnan Provincial Basic Research Program (No. 202201AU070178) and Yunnan Agricultural University Research Initiation Project (No. F2022-07) for the financial support of this research. Liyan Bi and Haoran Hu contributed equally in this study.

Author contributions
Liyan Bi and Xinran Liang wrote the main manuscript, Haoran Hu response the questions and modified the manucript in the revision. Lei Wang and Zuran Li did the experiment, Fangdong Zhan, Yonngmei He and Yanqun Zu prepared Figs. 1, 2, 3, 4, 5, 6, 7 and 8 and Yuan Li revised the manuscript. All authors read and approved the final manuscript.

Funding
This Project was funded by the Youth Project of Yunnan Provincial Basic Research Program under award number 202201AU070178 and Yunnan Agricultural University Research Initiation Project under award number No. F2022-07.

Data availability
No datasets were generated or analysed during the current study.

Declarations

Ethics approval and consent to participate
Not applicable.

Competing interests
The authors declare no competing interests.

Received: 22 February 2024 / Accepted: 26 August 2024
Published online: 28 September 2024

References

1. Qin Z, Yin H, Wang X, Zhang Q, Lan S, Koopal LK, Liu F (2018) The preferential retention of ^{VI}Zn over ^{IV}Zn on birnessite during dissolution/desorption. Appl Clay Sci 161:169–175
2. Ettler V, Knytl V, Komárek M, Della Puppa L, Bordas F, Mihaljevič M (2014) O. Šebek. Stability of a novel synthetic amorphous manganese oxide in contrasting soils. Geoderma 214–215:2–9
3. Cho KS, Talapin DV, Gaschler W (2005) Murray. Designing PbSe nanowires and nanorings through oriented attachment of nanoparticles. J Am Chem Soc 127(19):7140–7147
4. Shaughnessy DA, Nitsche H, Booth CH, Shuh DK, Waychunas GA, Wilson RE (2003) Serne. Molecular interfacial reactions between Pu (VI) and manganese oxide minerals manganite and hausmannite. Environ Sci Technol 37:3367–3374
5. Tebo BM, Bargar JR, Clement BG, Dick GJ, Murray KJ, Parker D, Webb SM (2004) Biogenic manganese oxides: properties and mechanisms of formation. Annu. Rev Earth Planet Sci 32:287–328
6. Cheng FY, Zhao JZ, Song WN, Li CH, Ma H, Chen J, Shen PW (2006) Facile controlled synthesis of MnO_2 nanostructures of Novel shapes and their application in batteries. Inorg Chem 45(5):2038–2044
7. Liang XR, Post JE, Lanson B, Wang X, Zhu MQ, Liu F, De Yoreo JJ (2020) Coupled morphological and structural evolution of δ-MnO_2 to α-MnO_2 through multistage oriented assembly processes: the role of Mn (III). Environ Science: Nano 7(1):238–249
8. Bera K, Karmakar A, Karthick K, Sankar SS, Kumaravel S, Madhu R, Kundu S (2021) Enhancement of the OER kinetics of the less-explored α-MnO_2 via nickel do approaches in alkaline medium. Inorg Chem 60(24):19429–19439
9. Li BX, Rong GX, Xie Y, Huang LF, Feng CQ (2006) Low-temperature synthesis of α-MnO_2 Hollow urchins and their application in Rechargeable Li^+ batteries. Inorg Chem 45(16):6404–6410
10. Diana ML, Mikaela RD, Killian RT, Wang L, Lisa MH, Yang SZ, Zhang BJ, Liu P, David CB, Zhu YM, Amy CM, Esther ST, Kenneth JT (2021) Local and Bulk Probe of Vanadium-substituted α-Manganese oxide (α-KxVyMn8–yO16) Lithium Electrochemistry. Inorg Chem 60(14):10398–10414
11. Yuan YF, Wood SM, He K, Yao W, Tompsett D, Lu J (2016) Shahbazian-Yassar, atomistic insights into the oriented attachment of tunnel-based oxide nanostructures. ACS Nano 10(1):539–548
12. Yang R, Fan Y, Ye R, Tang Y, Cao X, Yin Z, Zeng Z (2021) MnO_2-based materials for environmental applications. Adv Mater 33(9):2004862
13. Vodyanitskii YN (2009) Mineralogy and Geochemistry of Manganese: a review of publications. Eurasian Soil Sci 42(10):1170–1178
14. Yang RJ, Fan YY, Ye RQ, Tang Y, Cao X, Yin Z, Zeng Z (2021) MnO_2-based materials for environmental applications. Adv Mater 33(9):2004862
15. Suib SL (2008) Porous manganese oxide Octahedral Molecular sieves and Octahedral Layered materials. Acc Chem Res 41(4):479–487
16. Driehau W, Smith R, Jekel M (1995) Oxidation of arsenate (III) with manganese oxides in water treatment. Water Res 29:297–305
17. Grangeon S, Lanson B, Lanson M (2014) Solid-state transformation of nanocrystalline phyllomanganate into tectomanganate: influence of initial layer and interlayer structure. Acta Crystallogr Sect B: Struct Sci Cryst Eng Mater 70(5):828–838
18. Portehault D, Cassaignon S, Baudrin E, Jolivet JP (2007) Morphology control of cryptomelane type MnO_2 nanowires by soft chemistry. Growth mechanisms in aqueous medium. Chem Mater 19(22):5410–5417
19. Grangeon S, Fernandez-Martine A, Warmon F, Gloter A, Marty N, Poulain A, Lanson B (2015) Cryptomelane formation from nanocrystalline vernadite precursor: a high energy X-ray scattering and transmission electron microscopy perspective on reaction mechanisms. Geochem Trans 16:1–16
20. Lu A, Li Y, Ding H, Xu X, Li Y, Ren G, Hochella MF Jr (2019) Photoelectric conversion on Earth's surface via widespread Fe-and Mn-mineral coatings. Proc Natl Acad Sci 116(20):9741–9746
21. Liang X, Zhao Z, Zhu M, Liu F, Wang L, Yin H, Feng X (2017) Self-assembly of birnessite nanoflowers by staged three-dimensional oriented attachment. Environ Science: Nano 4(8):1656–1669
22. Liu J, Lei. Yu EY, Hu SG, Beth XQ, Yang P, Katharine (2018) Large-scale synthesis and comprehensive structure study of δ-MnO_2. Inorg Chem 57(12):6873–6882
23. Hummer DR, Golden JJ, Hystad G, Downs RT, Eleish A, Liu C, Ralph J, Morrison SM, Meyer M, Hazen RM (2022) Evidence for the oxidation of Earth's crust from the evolution of manganese minerals. Nat Commun 13(1):1–7
24. Suzuki K, Kato T, Fuchida S, Tokoro C (2020) Removal mechanisms of cadmium by δ-MnO_2 in adsorption and coprecipitation processes at pH 6. Chem Geol 550:119744
25. Post JE (1999) Manganese oxide minerals: Crystal structures and economic and environmental significance. Proc Natl Acad Sci USA 96:3447–3454
26. Kim JB, Dixon JB, Chusuei CC, Deng YJ (2002) Oxidation of chromium (III) to (VI) by Manganese Oxides. Soil Sci Soc Am J 66:306–315
27. Kohei S, Tatsuya K, Shigeshi F, Chiharu T (2020) Removal mechanisms of cadmium by δ-MnO_2 in adsorption and coprecipitation processes at pH6. Chem Geol 550:119744
28. Zhao HY, Zhu MQ, Li W, Elzinga EJ, Villalobos M, Liu MF, Sparks DL (2016) Redox reactions between Mn (II) and hexagonal birnessite change its layer symmetry. Environ Sci Technol 50(4):1750–1758

29. Elzinga EJ, Kustka AB (2015) A Mn-54 radiotracer study of mn isotope solid–liquid exchange during reductive transformation of vernadite (δ-MnO_2) by aqueous mn (II). Environ Sci Technol 49(7):4310–4316
30. Frierdich AJ, Spicuzza MJ, Scherer MM (2016) Oxygen isotope evidence for mn (II)-catalyzed recrystallization of manganite (γ-MnOOH). Environ Sci Technol 50(12):6374–6380
31. Wang Q, Liao XY, Xu WQ, Ren Y, Livi KJ, Zhu MQ (2016) Synthesis of birnessite in the presence of phosphate, silicate, or sulfate. Inorg Chem 55:10248–10258
32. Elzinga EJ (2011) Reductive transformation of birnessite by aqueous mn (II). Environ Sci Technol 45(15):6366–6372
33. Lefkowitz JP, Rouff AA, Elzinga EJ (2013) Influence of pH on the reductive transformation of birnessite by aqueous mn (II). Environ Sci Technol 47(18):10364–10371
34. Grangeon S, Lanson B, Lanson M (2014) Solid-state transformation of nanocrystalline phyllomanganate into tectomanganate: influence of initial layer and interlayer structure. Acta Crystallogr Sect B B70:828–8368
35. Yang P, Lee S, Post JE, Xu H, Wang Q, Xu W, Zhu M (2018) Trivalent manganese on vacancies triggers rapid transformation of layered to tunneled manganese oxides (TMOs): implications for occurrence of TMOs in low-temperature environment. Geochim Cosmochim Acta 240:173–190
36. De Yoreo JJ, Gilbert PUPA, Sommerdijk NAJM, Lee R, Penn (2015) Crystallization by particle attachment in synthetic, biogenic, and geologic environments. Science 349(6247):aaa6760
37. Zhang H, De Yoreo JJ, Banfield JF (2014) A unified description of attachment-based crystal growth. ACS Nano 8:6526–6530

Publisher's note